Supporting Information for "Defect Tolerance to Intolerance in the Vacancy-Ordered Double Perovskite Semiconductors Cs_2SnI_6 and Cs_2TeI_6"

Annalise E. Maughan,[†] Alex M. Ganose,[‡,¶] Mitchell M. Bordelon,[†] Elisa M. Miller,[§] David O. Scanlon,[‡,¶] and James R. Neilson[*,†]

[†]*Department of Chemistry, Colorado State University, Fort Collins, CO, 80523-1872, USA*

[‡]*University College London, Kathleen Lonsdale Materials Chemistry, Department of Chemistry, 20 Gordon Street, London WC1H 0AJ, UK*

[¶]*Diamond Light Source Ltd., Diamond House, Harwell Science and Innovation Campus, Didcot, Oxfordshire OX11 0DE, UK*

[§]*Chemical and Materials Sciences Center, National Renewable Energy Laboratory, 15013 Denver West Parkway, Golden, CO 80401, USA*

E-mail: james.neilson@colostate.edu

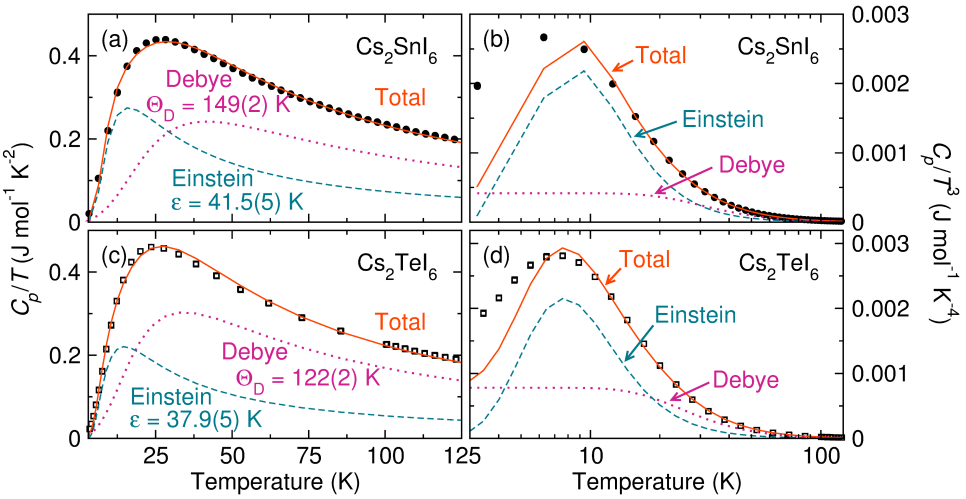

Figure S1: Heat capacity data of Cs_2SnI_6 (a,b) and Cs_2TeI_6 (c,d). The data are shown as filled black circles for Cs_2SnI_6 and open black squares for Cs_2TeI_6. The orange line is the total fit to the sum of the Debye and Einstein models of the heat capacity, and the separate contributions from each model are shown in pink dotted (Debye) and teal dashed (Einstein) lines. In (c) and (d) the data are shown at C_p/T^3 to highlight the deviation of the Debye model from the data at low temperatures.

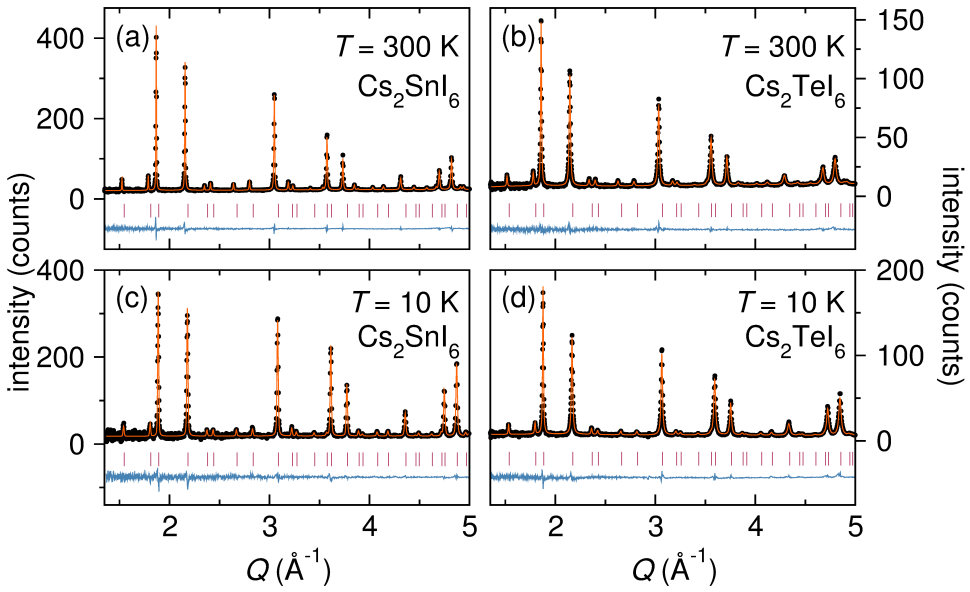

Figure S2: Rietveld refinements of high-resolution time-of-flight neutron scattering data of (a,c) Cs_2SnI_6 and (b,d) Cs_2TeI_6 collected from wavelength frame 4 of the POWGEN diffractometer at the Spallation Neutron Source, Oak Ridge National Laboratory. Data collected at $T = 300$ K are shown in panels (a) and (b) and data collected at $T = 10$ K are shown in (c) and (d). The structural models were refined jointly against data from wavelength frames 2 and 4. Black circles are the data, the orange line is the fit, and the blue line is the difference. The pink tick marks indicate the location of predicted Bragg reflections for the cubic structure.

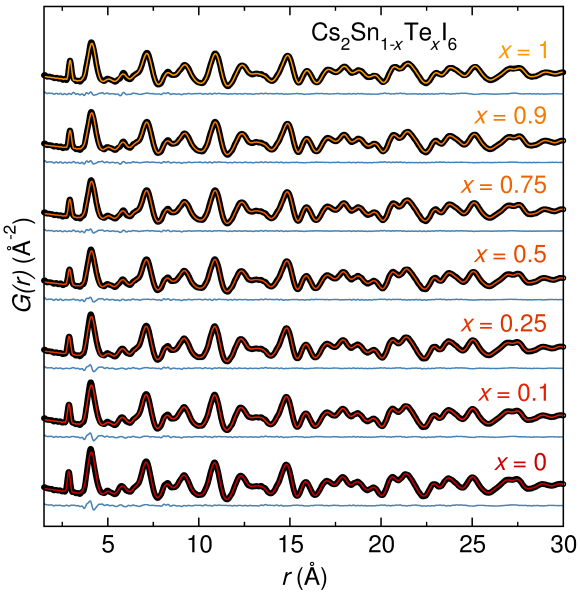

Figure S3: Structural modeling of the experimental X-ray pair distribution functions of $Cs_2Sn_{1-x}Te_xI_6$. Data are shown as black circles, the fits are colored lines, and the difference curves are shown as blue lines.

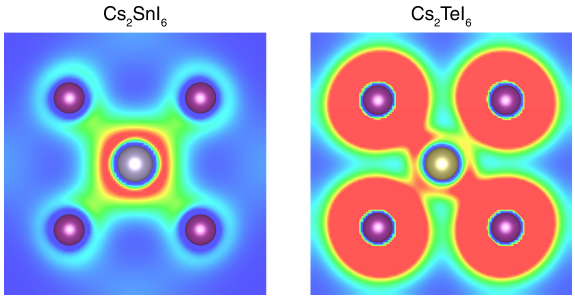

Figure S4: Charge density isosurfaces of the occupied ns^2 states in Cs_2SnI_6 and Cs_2TeI_6. Sn, Te, and I atoms are denoted by grey, gold, and purple spheres, respectively. Contours shown from 0 (blue) to 0.002 eV Å^{-3} and 0.0034 eV Å^{-3} (red) for Cs_2SnI_6 and Cs_2TeI_6, respectively

Geometry and electronic structure– The calculated structural and band gap data for Cs_2SnI_6 and Cs_2TeI_6 are given in given in Table SIII. The calculated lattice parameters are in keeping with previous studies performed using the HSE functional.[1,2] The effect of spin orbit coupling on the electronic properties of Cs_2SnI_6 and Cs_2TeI_6 was tested, with the full results provided in Figure S12. In both cases, the relativistic renormalization of the band gap occurs through raising of the valence band maximum by around $\sim$0.2 eV, with the conduction band remaining largely unaffected. The magnitude of this renormalization indicates that inclusion of spin orbit effects is essential to accurately model these systems, especially as the band degeneracy is influenced.

Table SI: LO-TO splitting (cm^{-1}) in the phonon spectrum of Cs_2SnI_6 and Cs_2TeI_6.

Cs_2SnI_6	0.3, 3.4, 9.4, 10.8, 20.7
Cs_2TeI_6	0.3, 4.2, 11.6, 14.9

Table SII: Dielectric constant and Born effective charges on MIV calculated both with and without spin orbit coupling effects.

	Cs_2SnI_6		Cs_2TeI_6	
	PBEsol	PBEsol+SOC	PBEsol	PBEsol+SOC
$\varepsilon^{\infty}_{xx}$	5.5	4.6	6.2	5.0
Z^{*}_{xx}	3.9	3.3	4.4	4.1

Table SIII: Calculated geometric and electronic structure data for Cs_2SnI_6 and Cs_2TeI_6. The lattice parameters and cation–anion interatomic distances were calculated using HSE06 and are quoted in Å. All cell angles were found to be 90°. The equilibrium crystal structures can be found online in a public repository.[3] E_g^{dir} and E_g^{ind} are the direct and indirect band gaps, respectively, calculated using HSE06+SOC and given in eV.

	Cs_2SnI_6	Cs_2TeI_6
a	11.96	11.98
$d_{\mathrm{M^{IV}-I}}$	2.87	2.94
$d_{\mathrm{M^{IV}-Cs}}$	5.18	5.19
$d_{\mathrm{I-I}}$	4.40	4.32
E_g^{dir}	0.97	2.05
E_g^{ind}	—	1.83

Optical spectroscopy– The optical gaps for each compound in the solid solution were determined by a variety of methods to highlight the ambiguity in determination of the band gap from optical spectroscopy. First, lines were fit to the baseline and to the onset region of the raw reflectance data; the optical gaps were determined by their intersection. These values are represented as orange circles in Figure 7. Other values for the optical gaps were extracted by transforming the raw reflectance data to the Kubelka-Munk function, F(R), (as shown in Figure S6). A fitted line in the onset region was extrapolated to zero absorbance. Additionally, the data were converted from reflectance to absorbance and normalized from hν = 1.25–4 eV. A line was fit to the onset region and extrapolated to zero absorbance. The range of values obtained by these different methods are represented by the blue bars in Figure 7.

Electric dipole allowed and disallowed transitions were calculated from the magnitude of matrix element square, $|M|^2$. Transitions were considered allowed if $|M|^2 > 10^{-3}\,\mathrm{eV^{-2}\AA^{-2}}$, otherwise they were determined to be symmetry disallowed. The transition matrix elements were calculated using HSE06 with explicit treatment of spin-orbit coupling effects. In Cs_2SnI_6, analysis of the direct VB-CB transitions indicates that the transition from the twofold degenerate VBM to the CBM at Γ is dipole forbidden. This effect is well known in materials whose crystal structures possess a center of inversion,[4–6] as strong optical transitions are only permitted between states of opposing parity. Transitions from the doubly degenerate bands 0.02 eV beneath the VBM were also found

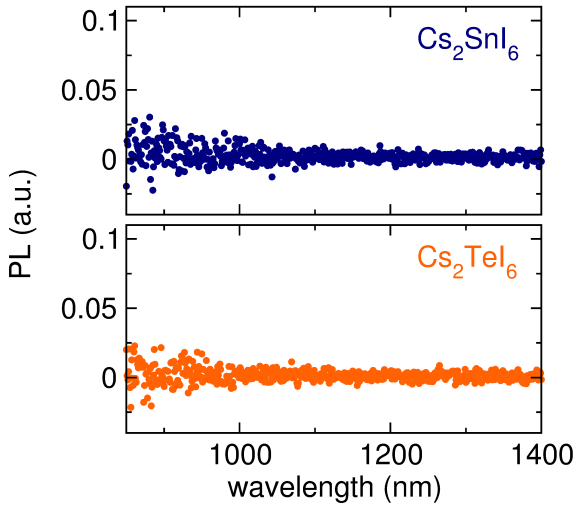

Figure S5: Room-temperature photoluminescence (PL) measurements of (a) Cs_2SnI_6 and (b) Cs_2TeI_6.

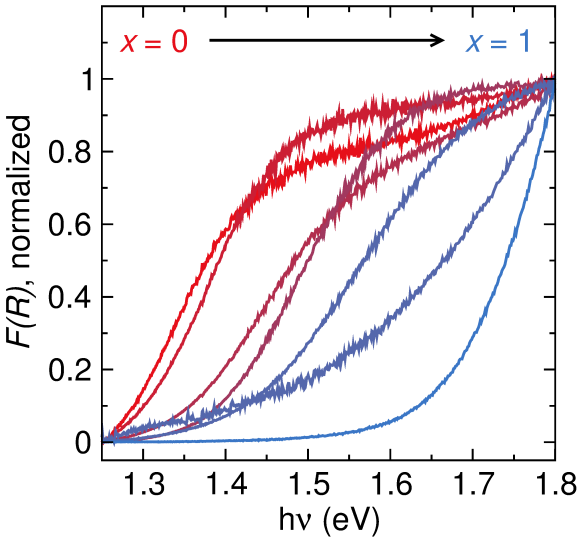

Figure S6: UV-visible diffuse reflectance data for the solid solution series plotted as the normalized Kubelka-Munk function, $F(R)$ vs. photon energy (hν).

to be dipole disallowed. It is only from 0.35 eV below the VBM (from the VB-4) that strong transitions are observed, resulting in a fundamental allowed optical band gap of 1.33 eV (illustrated in Figure S8).

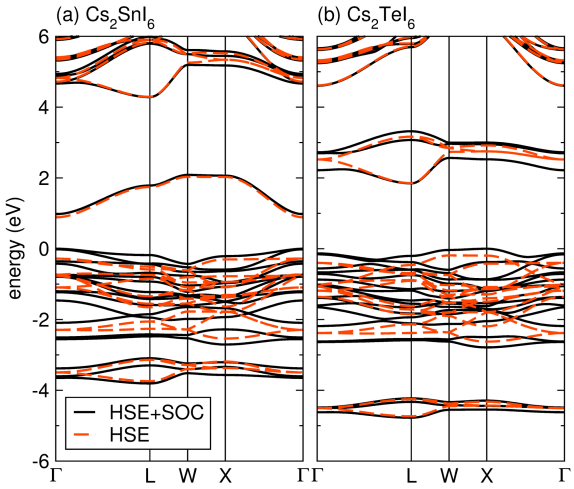

Figure S7: Relativistic renormalization effect on the band structures of (a) Cs_2SnI_6 and (b) Cs_2TeI_6. The HSE+SOC band structure is shown in black with the HSE only band structure shown via dashed red lines.

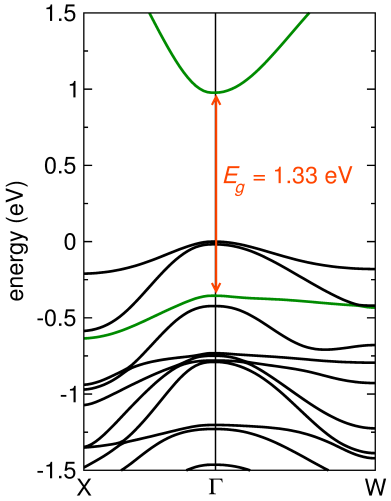

Figure S8: Band structure of Cs_2SnI_6 depicting the fundamental band gap at Γ. The bands resulting in the fundamental allowed optical band gap are indicated in green. The valence band maximum is set to 0 eV.

Band Alignments– The Fermi level determined by XPS ($\phi = 4.43$ eV, Figure S11) resides $\sim$0.52 eV above the conduction band minimum, which would suggest that the material is degenerately *n*-type, which is consistent with Hall measurements of this material. However, the position of the Fermi level relative to the conduction band minimum would suggest a 1000-fold increase in carrier concentration relative to $n_e = 5 \times 10^{16}$ determined experimentally. This discrepancy may arise from the trapping of a significant number of carriers in grain boundaries; however, it is more

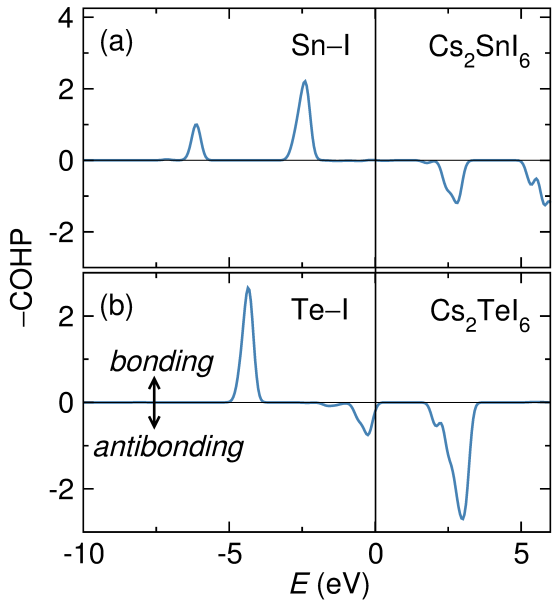

Figure S9: Crystal orbital Hamilton population (COHP) analysis of (a) Cs_2SnI_6 and (b) Cs_2TeI_6, in which the density of states is partitioned for Sn–I and Te–I interactions, with the sign indicating bonding or antibonding character, and the magnitude related to the strength of the interaction. The valence band maximum is set to 0 eV.

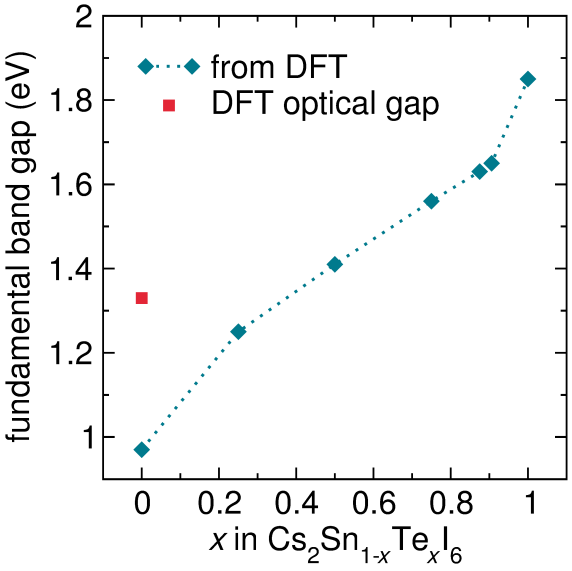

Figure S10: Fundamental band gaps calculated using HSE06+SOC for several members of the solid solution. The calculated dipole-allowed optical transition for Cs_2SnI_6 is shown as a red square for reference.

likely to arise from the surface sensitivity of the XPS measurements. As such, the non-ideal surface stoichiometry (Cs:Sn:I = 1.5:1:4) likely reflects the electronic behavior of the sample surface

and may not be entirely reflective of the bulk material.

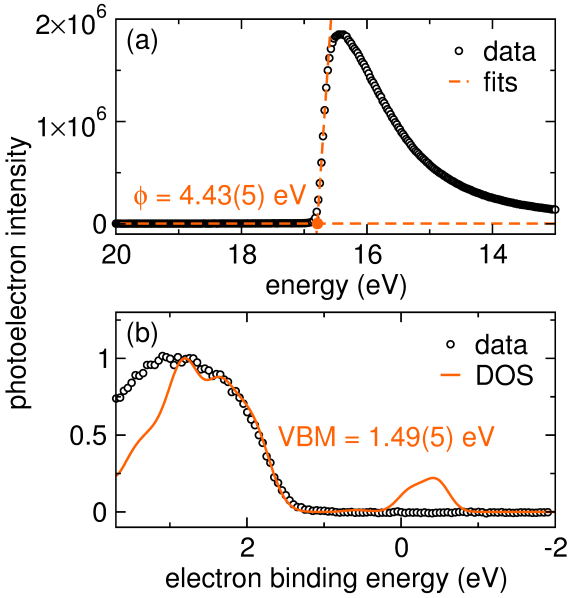

Figure S11: X-ray photoelectron spectroscopy data for Cs_2SnI_6. (a) The work function is extrapolated from the secondary electron cutoff. (b) The DOS convoluted with a 350 meV Gaussian allows interpolation of the XPS data to yield the valence band maximum with respect to Fermi level.

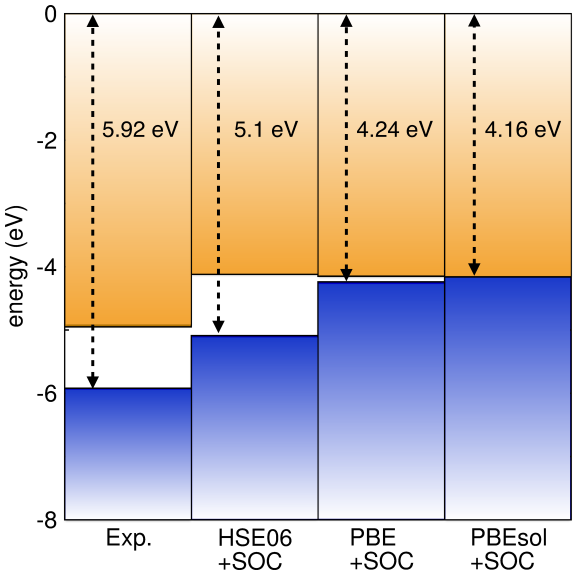

Figure S12: Band alignments for Cs_2SnI_6 from XPS analysis compared to calculated band alignments using HSE06+SOC, PBE+SOC, and PBESol+SOC. The vacuum level is set to 0 eV.

Defects– Through varying the chemical potentials, μ_i, we can simulate the effect of experimentally varying the partial pressures in the formation of Cs_2SnI_6 and Cs_2TeI_6. These potentials are defined within the global constraint of the calculated enthalpy of the host, in this case: Cs_2SnI_6: $2\mu_{Cs} + \mu_{Sn} = \Delta H_f^{Cs_2SnI_6}$ and Cs_2TeI_6: $2\mu_{Cs} + \mu_{Te} = \Delta H_f^{Cs_2TeI_6}$. To avoid precipitation into solid elemental Cs, I, and Sn or Te, we also require $\mu_{Cs} \leq 0$, $\mu_I \leq 0$, $\mu_{Sn} \leq 0$, and $\mu_{Te} \leq 0$. Lastly, the chemical potentials are further constrained in order to avoid decomposition into a range of binary and ternary compounds. In the case of Cs_2SnI_6 these are: $\mu_{Cs} + \mu_{Sn} + 3\mu_I = \Delta H_f^{CsSnI_3}$, $\mu_{Sn} + 4\mu_I = \Delta H_f^{SnI_4}$, $\mu_{Cs} + \mu_I = \Delta H_f^{CsI}$, and $\mu_{Cs} + 3\mu_I = \Delta H_f^{CsI_3}$. On the other hand, Cs_2TeI_6 is limited by: $\mu_{Cs} + 4\mu_I = \Delta H_f^{CsI_4}$, $\mu_{Cs} + 3\mu_I = \Delta H_f^{CsI_3}$, $\mu_{Cs} + \mu_I = \Delta H_f^{CsI}$, and $\mu_{Te} + 4\mu_I = \Delta H_f^{TeI_4}$. The full list of limits considered along with their calculated formation energies is provided in Table SIV.

The accessible range of chemical potentials for Cs_2SnI_6 and Cs_2TeI_6, are shown in Figure S13, in a two-dimensional (μ_{Cs}, μ_{Te}) plane.[7,8] The stability field is limited by the host conditions ($2\mu_{Cs} + \mu_{Sn} = \Delta H_f^{Cs_2SnI_6}$ and $2\mu_{Cs} + \mu_{Te} = \Delta H_f^{Cs_2TeI_6}$) to give the limits of Cs/Sn rich, Cs poor, and Sn poor environments for Cs_2SnI_6 and analogous environments for Cs_2TeI_6. Taking into account the limits imposed by the competing binary and ternary phases results in the stable ranges shaded in orange. The stable range of chemical potential space is significantly larger for Cs_2TeI_6, indicating that the formation of Cs_2SnI_6 will have greater sensitivity to the equilibrium reaction conditions. Within these boundaries we have highlighted several environments, termed A to E, which correspond to a range of Cs-poor, Sn/Te-rich, and I-poor conditions. In both cases we have explicitly considered the chemical potentials of the C point as a representative middle ground for calculating the defect formation energies, however it is the B point which is expected to most favor the formation of *n*-type V_I defects.

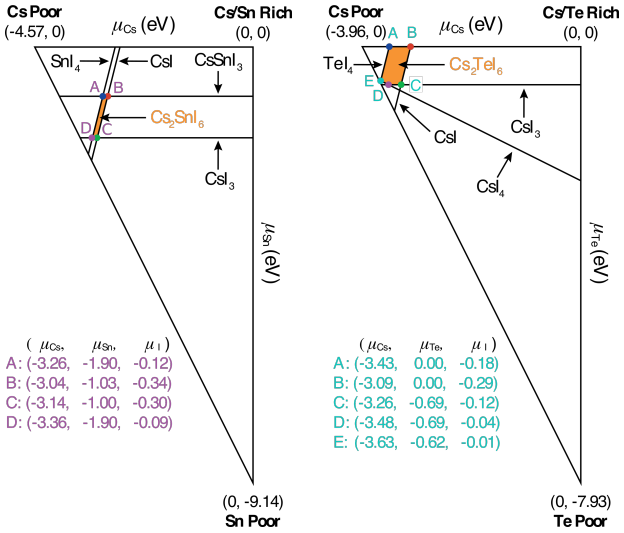

Figure S13: Illustration of the accessible chemical potential ranges of (a) Cs_2SnI_6 and (b) Cs_2TeI_6. Constraints imposed by the formation of competing binary and ternary compounds result in the stable region indicated in orange.

Table SIV: Full list of competing phases considered when calculating the chemical potential space of Cs_2SnI_6 and Cs_2TeI_6, along with their corresponding formation energies in eV.

Limit	$\Delta H_f(eV)$
Cs_2Te	–3.373
Cs_2Te_{13}	–4.507
Cs_2Te_3	–4.251
Cs_4Sn_{23}	–3.868
CsSn	–0.658
$CsSnI_3$	–5.084
CsTe	–1.957
SnI_2	–1.510
SnI_4	–2.244
TeI	–0.178
TeI_4	–0.652
CsI	–3.379
CsI_3	–3.617
CsI_4	–3.661
TeI_2	–0.118
Te_2I	–0.165

References

(1) Xiao, Z.; Hosono, H.; Kamiya, T. *Bull. Chem. Soc. Jpn.* **2015**, *88*, 1250–1255.

(2) Xiao, Z.; Zhou, Y.; Hosono, H.; Kamiya, T. *Phys. Chem. Chem. Phys.* **2015**, *17*, 18900–18903.

(3) `https://github.com/SMTG-UCL/CSI-CTI`, Accessed: 2016-02-01.

(4) Walsh, A.; Da Silva, J. L.; Wei, S.-H.; Körber, C.; Klein, A.; Piper, L.; DeMasi, A.; Smith, K. E.; Panaccione, G.; Torelli, P. *Phys. Rev. Lett.* **2008**, *100*, 167402.

(5) Kehoe, A. B.; Scanlon, D. O.; Watson, G. W. *Phys. Rev. B* **2011**, *83*, 233202.

(6) Godinho, K. G.; Carey, J. J.; Morgan, B. J.; Scanlon, D. O.; Watson, G. W. *J. Mater. Chem.* **2010**, *20*, 1086–1096.

(7) Persson, C.; Zhao, Y.-J.; Lany, S.; Zunger, A. *Phys. Rev. B* **2005**, *72*, 035211.

(8) Scanlon, D. O. *Phys. Rev. B* **2013**, *87*, 161201.